

# deep-REMAP: Probabilistic Parameterization of Stellar Spectra Using Regularized Multi-Task Learning

Sankalp Gilda<sup>1</sup>★

<sup>1</sup>DeepThought Solutions, FL, USA

Accepted 08/10/2025. Received 30/09/2025; in original form 12/01/2024

## ABSTRACT

In the era of exploding survey volumes, traditional methods of spectroscopic analysis are being pushed to their limits. In response, we develop deep-REMAP, a novel deep learning framework that utilizes a regularized, multi-task approach to predict stellar atmospheric parameters from observed spectra. We train a deep convolutional neural network on the PHOENIX synthetic spectral library (Husser et al. 2013) and use transfer learning to fine-tune the model on a small subset of observed FGK dwarf spectra from the MARVELS survey (Ge et al. 2008). We then apply the model to 732 uncharacterized FGK giant candidates from the same survey. When validated on 30 MARVELS calibration stars, deep-REMAP accurately recovers the effective temperature ( $T_{\text{eff}}$ ), surface gravity ( $\log g$ ), and metallicity ([Fe/H]), achieving a precision of, for instance, approximately 75 K in  $T_{\text{eff}}$ . By combining an asymmetric loss function with an embedding loss, our regression-as-classification framework is interpretable, robust to parameter imbalances, and capable of capturing non-Gaussian uncertainties. While developed for MARVELS, the deep-REMAP framework is extensible to other surveys and synthetic libraries, demonstrating a powerful and automated pathway for stellar characterization.

**Key words:** stars: fundamental parameters – methods: data analysis – techniques: spectroscopic – astronomical data bases – catalogues

## 1 INTRODUCTION

In the last few decades, computers have revolutionized astronomy. The emergence of novel and complex instruments, advances in telescope designs allowing for ever larger apertures, and increased private and public funding have enabled us to not only exponentially expand survey volumes, but also to observe objects with unprecedented resolution. Just within the Sloan Digital Sky Survey (SDSS, York et al. 2000; Eisenstein et al. 2011), various large-scale sky survey programs such as the Sloan Extension for Galactic Understanding and Exploration (SEGUE, Yanny et al. 2009), RAdial Velocity Experiment (RAVE, Kordopatis et al. 2013), Baryon Oscillation Spectroscopic Survey (BOSS, Dawson et al. 2012), and the Large Sky Area Multi-Object Fiber Spectroscopic Telescope Telescope (LAMOST, Cui et al. 2012) have collected spectra for hundreds of thousands to millions of stars. Massive data releases like those from the Gaia-ESO Survey (Gilmore et al. 2012), the Dark Energy Survey Instrument (DESI, Levi et al. 2013), and the Large Synoptic Sky Survey (LSST, Ivezić et al. 2019) will not only add to the corpus of data, but will demand significant computational resources for subsequent analysis. Modern methods in machine learning and statistics are playing an increasingly important role in

virtually all fields of astronomy—deep learning (DL) frameworks have been developed and utilized in star-galaxy classification (Kim & Brunner 2016), photometric redshift prediction (Hoyle 2016), identification of galaxy-galaxy strong lensing (Lanusse et al. 2017), and analysis of survey data products (Mahabal et al. 2019), to name a few applications.

Specifically with respect to spectral analysis, this new wave of automation has offered many alternatives to help overcome limitations of the conventional methods. Accurate stellar characterization is essential not only for understanding stellar evolution but also for applications such as exoplanet detection via radial velocity methods (Ma et al. 2018), where stellar parameters directly impact derived planetary properties.

One such widely used method for determination of stellar atmospheric parameters from absorption spectra (henceforth ‘stellar parameterization’) is the ‘Equivalent Widths (EW) Method’, detailed in Sousa (2014). Although a powerful technique for high resolution data (Valenti & Fischer 2005), it fails to parameterize low to moderate resolution spectra due to the blending of spectral lines. The commonly used technique in such cases is spectral synthesis, which involves the determination of stellar parameters through a comparison of an observed spectrum with an extensive library of synthetic ones. This has been widely used in data analysis pipelines for several surveys, such as SEGUE (Lee et al. 2008; Smolinski et al. 2011), RAVE (Kordopatis et al. 2013), LAMOST

★ E-mail: sankalp.gilda@gmail.com. This paper has been accepted for publication in MNRAS.

(Cui et al. 2012) and AMBRE (De Laverny et al. 2012; Worley et al. 2012). Some of the drawbacks of this method (Ghezzi et al. 2014) include a dependency on the completeness and accuracy of atomic line databases, and the need to accurately determine broadening parameters (instrument profile, macro turbulence, and rotational velocities). To combat this issue, Ghezzi et al. (2014) developed and utilized spectral indices—specific spectral regions combining multiple absorption lines into broad, blended features. However, this method has its own set of limitations, primarily that for a given survey, it requires the user to calculate and input a list of spectral indices and their respective equivalent widths. These methods, in addition, are also data-inefficient, in that they only consider certain parts of a given spectrum while assigning little importance to the rest.

Successful and efficient interpretation of large-scale, high-dimensional spectral data, in the presence of the above mentioned limitations of the conventional methods, has forced us to embrace advances in informatics. The past decade and a half alone alone has seen the development of several machine learning (ML) based algorithms for stellar parameterization—from simple ones that use multi layer perceptrons (MLPs; simple sequences of fully connected layers, (Bailer-Jones 2000; Snider et al. 2001; Manteiga et al. 2010)) to more sophisticated ones based on convolutional neural networks (CNNs), such as “The Cannon” (Ness et al. 2015), “The Cannon 2” (Casey et al. 2016), “The Payne” (Ting et al. 2018), “StarNet” (Bialek et al. 2019), Xiang et al. (2016)’s work on stellar parameter prediction using Principal Component Analysis, and Sharma et al. (2019)’s work on predicting stellar spectral type by leveraging semi-supervised learning, and Gilda et al. (2021b) who developed an ML framework for SED modeling. While promising steps in the right direction, these works either use simple networks incapable of capturing the complicated relationships between spectra and stellar parameters, require large amount of already labeled data from a given survey to parameterize newly observed stars, and/or are restricted to the range of stellar parameters available for the training data (i.e., do not generalize to out of sample distributions). In this work, we develop deep – REMAP—a novel, interpretable, state-of-the-art neural network capable of overcoming these limitations. We maximize its performance by leveraging the most advanced training practices, routines, and loss functions in the deep learning (DL) literature. We apply our network to one-dimensional (1D) spectra from the MARVELS survey (Ge et al. 2008), validate its skill on stars with known atmospheric parameters, and for the first time predict these values ( $T_{\text{eff}}$ ,  $\log g$ , [Fe/H]) for 732 FGK giant star candidates.

Recent advances have begun addressing the synthetic-observational mismatch more systematically. O’Briain et al. (2021) introduced Cycle-StarNet, using unsupervised domain adaptation to bridge the gap between synthetic and observed spectra. For low-resolution spectra, Li et al. (2024) developed AspGap, successfully applying transfer learning from APOGEE to Gaia XP spectra. Leung et al. (2023) demonstrated transfer learning’s efficacy for spectroscopic age estimation. However, moderate-resolution spectra like MARVELS ( $R \sim 11,000$ ) present unique challenges – line blending precludes traditional EW methods while the resolution remains insufficient for standard high-resolution ML approaches. This necessitates the careful combination of transfer learning and probabilistic frameworks we present in this work.

The rest of this paper is organized as follows: In §2 we briefly describe convolutional neural networks with a specific focus on the architecture of deep – REMAP. In §3 we characterize both MARVELS and synthetic PHOENIX spectral data, and delineate the

pre-processing steps undertaken before both sets of spectra are input into the neural network. In §4.1 through §4.7, we outline the various state-of-the-art modules and training practices used in this paper to improve our network’s performance. In §5 we sketch out in detail our training routine, loss functions, and model hyperparameters. In §6 we showcase deep – REMAP’s performance on predicting the three stellar parameters, both for the synthetic and real MARVELS spectra. We also breakdown the model skill as a function of the various methods described in §4, thus highlighting their importance and justifying their inclusion in our model. Finally, in §7 we summarize our work and suggest possible routes of inquiry for future research endeavors in this space. In brief, our key contributions are as follows.

- (i) We demonstrate the necessity and successful implementation of transfer learning to better map synthetic libraries to real observations.
- (ii) We utilize and demonstrate the effectiveness of many state-of-the-art methods increasingly common in several applications of deep learning, but missing in the astronomical literature.
- (iii) We show that by converting a regression problem to a classification one, switching the softmax loss function to one better able of handing imbalanced classes, and regularizing it with an embedding loss, our network is not only able to work with random probability distributions, but is also interpretable by being able to retrieve nearest neighbors for any given query spectrum.
- (iv) We predict, for the first time, the stellar parameters (and related uncertainties) for 732 suspected MARVELS red giant stars.

## 2 CONVOLUTIONAL NEURAL NETWORKS

Convolutional Neural Networks (CNNs, e.g. LeCun et al. 1998; Krizhevsky et al. 2012; Szegedy et al. 2016) are a class of artificial neural networks used in image recognition and processing that are specialized for application on pixel and voxel-based data. They consist of an input layer, an output layer, and one or more hidden layers (a CNN with more than one hidden layer is referred to as a Deep CNN, or a DCNN). Over many cycles (or *epochs*) the network learns the convolutional filters, weights (or *kernels*), and biases necessary to extract meaningful patterns from the input image. For an input image, a DCNN assigns importance to various aspects/objects in it, and tries to map them to the output label of choice in a way that minimizes the user-defined *loss-function*. Compared to other image processing algorithms, DCNNs require very little pre-processing of the input images (such as creation of hand-crafted features); with enough training, the filters of a DCNN have the ability to extract relevant features for classification or regression tasks. Through the application (*activations*) of its filters, a DCNN is thus able to successfully capture the spatial dependencies in an image. It has fewer parameters and more sophistication than a multi-layer perceptron, and is a far superior choice for handling images, especially at scale. (See also Schmidhuber 2015, Bengio et al. 2017, and references therein for a comprehensive introduction to neural networks).

The deep – REMAP architecture is illustrated in Figure 1. It consists of several *residual modules*, batch-normalization layers and dropout layers for regularization (Ioffe & Szegedy 2015; Srivastava et al. 2014), and parallel mean and max pooling layers for feature extraction and reduction of overfitting (Lin et al. 2013). Residual modules were introduced in He et al. (2016) as part of the widely used ResNet architecture. Depicted in Figure 1 (left panel), the residual module comes in two flavors: the *identity residual module* and the *projection residual module*. The former is a block of two

convolutional layers with the same number of filters and a small filter size, where the output of the second layer is added with the input to the first convolutional layer. The latter uses strides to reduce the size of the input image, and adds more filters. We also use three sets of *heads* for extracting features specific to each of the three parameters, and making predictions using them—all while taking the parameters’ mutual interdependence into account. Each of these heads in turn consist of two sub-heads for two different types of losses—a *classification loss* and an *embedding loss* (see §4 for details).

In addition, we also identify a few choices that are critical in obtaining the results reported in §6:

(i) We use the state-of-the-art Mish activation function (Misra 2019). We find that this significantly speeds up training compared to both ReLU (Hahnloser et al. 2000; Nair & Hinton 2010; Glorot et al. 2011) and Leaky ReLU (Maas et al. 2013).

(ii) We use both global average pooling and global max pooling. We find that using both, we are able to capture more informational deep features than with either one of the pooling schemes alone.

For each of the three stellar parameters, we use the focal-loss (Lin et al. 2017) as the classification loss, and the triplet-loss (Chechik et al. 2010; Schroff et al. 2015; Hoffer & Ailon 2015; Hermans et al. 2017) as the embedding loss. We iteratively update the model weights using the ‘Adam’ optimizer (Kingma & Ba 2014). We bin the real-valued variables  $T_{\text{eff}}$ ,  $\log g$ , and  $[\text{Fe}/\text{H}]$  using the median values of the distributions of their respective uncertainties, and use *one-hot encoding* (aka *one-of- $K$  encoding*) to convert those real-valued bins into binary values<sup>1</sup>. The output predictions are converted back to numerical bins. Details about one-hot encoding and decoding, loss function creation, and the training scheme and are discussed in §4.

### 3 DATA AND PRE-PROCESSING

#### 3.1 MARVELS Spectra

In this work we use spectra from the Sloan Digital Sky Survey III (SDSS-III, Eisenstein et al. 2011) Multi-object APO Radial Velocity Exoplanet Large-area Survey (MARVELS, Ge et al. 2008) taken with the SDSS 2.5-m telescope at the Apache Point Observatory (Gunn et al. 2006). Between October 2008 and July 2009, using a fibre-fed dispersed fixed delay interferometer (DFDI) and a medium resolution ( $R \sim 11,000$ , Ge et al. 2009) spectrograph, MARVELS observed  $\sim 5,500$  stars with a goal of characterizing short-to-intermediate period giant planets in a large and homogeneous sample of FGK dwarfs. Grieves et al. (2017) compared the MARVELS radial velocity results from the University of Florida Two Dimensional (UF2D, Thomas 2015) data processing pipeline to results from the University of Florida One Dimensional (UF1D, Thomas et al. 2016) pipeline, while Alam et al. (2015) presented an overview of previous MARVELS data reductions. Paegert et al. (2015) describes the MARVELS target selection process, along with the ineffective giant star removal method which resulted in  $\sim 24\%$  giant contamination rate.

As mentioned in §1, Ghezzi et al. (2014) developed the spectral

<sup>1</sup> For instance, if one were aiming to classify the color of a flower as either white, red or orange, one version of *one-hot encoding* these would be: white→[1,0,0], red→[0,1,0], and orange→[0,0,1]

indices method as an alternative approach to the spectral synthesis technique to obtain accurate atmospheric parameters for low to moderate resolution spectra. They tested the method specifically for MARVELS with a validation sample of 30 MARVELS stars that had high resolution spectra obtained from other instruments. Each MARVELS star has two sets of spectra due to the interferometer which creates two “beams”. Each set of spectra are analyzed separately and two sets of parameters for each star are combined using a simple average and uncertainties are obtained through an error propagation. Grieves et al. (2018) expanded the application of this method further and derive stellar parameters for all  $\sim 5,500$  observed stars. They applied certain cuts based on number of observations per star ( $\geq 10$ ), quality of observations (poor or missing observations caused by dead or mis-plugged fibers, spectra suggesting the star is a spectroscopic binary, or unreasonable photon errors), and uniqueness of stars (they identify 7 duplicates). This culling leaves 3,075 unique stars, which are then further divided into dwarfs+subgiants and giants. This is because the spectral indices pipeline was designed specifically for a certain range of stellar parameters— $4,700 \text{ K} \leq T_{\text{eff}} \leq 6,000 \text{ K}$ ,  $3.5 \leq \log g \leq 4.7$ , and  $-0.9 \leq [\text{Fe}/\text{H}] \leq 0.5$ . The resulting 2,540 dwarfs+subgiants were subsequently winnowed down to 2,343 dwarfs based on the definition from Ciardi et al. (2011) (see §3 in Grieves et al. 2018 for more details).

We use the stellar parameters (and associated uncertainties) of 2,313 of these stars (Nolan Grieves, private communication) to fine-tune our network, validate its performance on the remaining 30 calibration stars, and use it to predict the parameters for the residual 732 giant and sub-giant candidate stars.

#### 3.2 PHOENIX Spectra

The PHOENIX grid of synthetic spectra (Husser et al. 2013) was created for high resolution ( $R \geq 100,000$ ) stellar spectra spanning ultra-violet to infrared wavelengths (50–5,000 nm). It spans a large parameter space ( $2,300 \leq T_{\text{eff}} \leq 12,000 \text{ K}$ ,  $0 \leq \log g \leq 6$ ,  $-4 \leq [\text{Fe}/\text{H}] \leq 1$ ,  $-0.2 \leq [\alpha/\text{Fe}] \leq 1.2$ ). In this work, we consider only the subset of PHOENIX grid relevant to the MARVELS parameter space. Since MARVELS stars are expected to be F,G and K type stars, we limit the PHOENIX stellar parameter to:  $4,850 \leq \lambda \leq 5,750 \text{ \AA}$ ,  $3,000 \leq T_{\text{eff}} \leq 7,000 \text{ K}$ ,  $1.0 \leq \log g \leq 5.5$ ,  $-2 \leq [\text{Fe}/\text{H}] \leq 1$ . Below, we describe how the synthetic PHOENIX spectra are brought in line with MARVELS spectra to reduce the discrepancies between them, thus allowing for successful transfer learning.

#### 3.3 Pre-processing and Data Augmentation

Synthetic spectra are typically created to either be commensurate with observed spectra from a particular survey, or at least to reproduce their major absorption features. For instance, the INTRIGOSS (Franchini et al. 2018) synthetic grid was tuned by direct comparison to Gaia-ESO spectra of FGK stars. Similarly, Husser et al. (2013) used PHOENIX to analyse MUSE integral field spectra of stars in the metal-poor globular cluster NGC 6397. Thus to be able to use such a synthetic grid for analysis of real observed spectra for which it was not designed, we have to take special care to traverse the *synthetic gap*. This refers to the differences in the shapes, depths, and number of absorption lines between the two sets, arising due to both instrumental and observational effects. To this end, we make the following changes to the the subset of PHOENIX spectra selected in §3.2, in the described order:

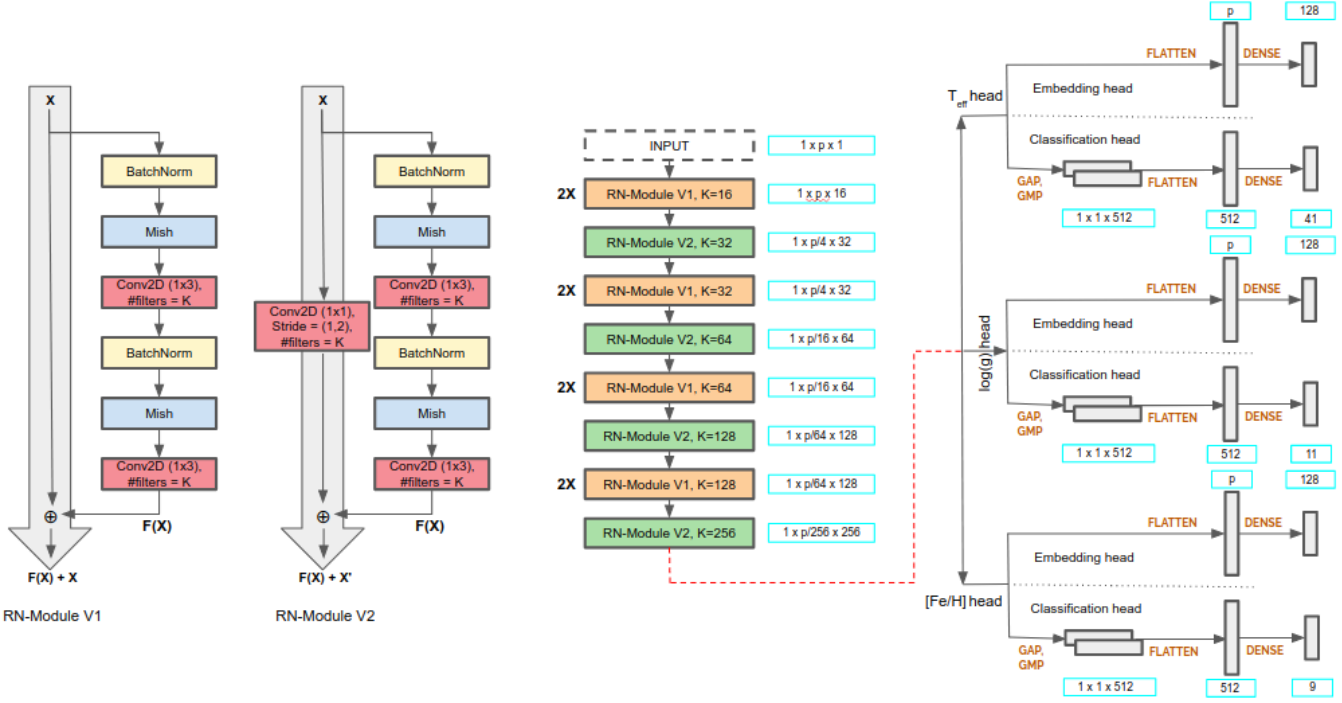


**Figure 1.** Schematic of the deep – REMAP neural network architecture. **Left:** The structure of the two types of residual modules used, RN-Module V1 (identity) and V2 (projection for downsampling). **Middle:** The network backbone, consisting of a sequence of residual modules that progressively increase the feature depth ( $K$ ) while reducing the spectral dimension ( $p$ ). **Right:** The multi-task head structure. The shared feature backbone splits into three parallel heads, one for each stellar parameter ( $T_{\text{eff}}$ ,  $\log g$ ,  $[\text{Fe}/\text{H}]$ ). Each head further splits into an *embedding head* (trained with triplet loss) to structure the latent space, and a *classification head* (trained with focal loss) to produce the final probabilistic prediction.

(i) Down-convolution: We convolve PHOENIX spectra with three Gaussian kernels to reduce their resolution from 100,000 to 10,000, 11,000 and 12,000; this is to account for the resolution-variation across CCD elements.

(ii) Resampling: We resample PHOENIX spectra onto the wavelength grid of MARVELS via cubic spline interpolation; this reduces the wavelength spacing from 0.01 to 0.1 Å.

(iii) Noise Addition: We add Gaussian noise to all PHOENIX spectra with the constraint  $0.5\% \leq \sigma \leq 2\%$ , corresponding to the Signal-to-Noise (SNR) distribution of the majority of MARVELS spectra ( $50 \leq \text{SNR} \leq 200$ ). At such high values of SNR, Gaussian noise is a very good substitute for Poisson noise. We uniformly choose five different values of  $\sigma$  in the above range, and sample thrice for each of the five values.

(iv) Continuum Normalization: We remove the continuum from both PHOENIX and MARVELS data via the same method (described below) for consistency.

All the above steps constitute *pre-processing*—making synthetic data ready for use with deep – REMAP—while steps (i) and (iii) also constitute *data augmentation*. The latter is a very common method used in ML and DL applications, where we create new samples to both increase the size of the training set (deep neural networks are notoriously data hungry), and to make the model robust to variations expected in real data. Since we know that MARVELS spectra have varying resolutions with wavelength, and varying noise levels due to different number of spectra stacked to produce the final spectrum for each star, we introduce this information in the ‘vanilla’ PHOENIX spectra.

**Continuum Normalization:** Continuum estimation and removal is a key component in spectroscopic analysis. While several methods exist in literature—polynomial fitting to either the whole or part of the spectrum (Casey et al. 2016; Pérez et al. 2016), sigma clipping (Bialek et al. 2019), smoothing with a Gaussian kernel (Ho et al. 2017)—in this work we develop a novel routine (described in Algorithm 1). Extensive testing on synthetic spectra spanning a large parameter space, and injected with various levels of noise, demonstrated the effectiveness of our algorithm. In future, we plan on comparing the performance and efficiency of our continuum normalization scheme with more advanced algorithms in literature, such as those based on the wavelet transform (Zhao & Luo 2006), the framelet transform (Wang et al. 2010), and a combination of the wavelet transform with Kalman filtering (Gilda & Slepian 2019) for simultaneous signal denoising and continuum removal.

Like with any real spectra, the 3,075 unique MARVELS spectra need careful consideration before we can accurately estimate their continuum levels. Firstly, we identify and remove traces of *fake features* from the combined 2D spectra before collapsing them to 1D. These include cosmic rays and interferometric signatures:  $\sim 20\%$  MARVELS spectra contain bright features that can span up to six pixels ( $\approx 1 \text{ \AA}$  in width) (Grieves et al. 2017, 2018). These features remain stationary (in wavelength space) throughout the time-span of the survey, which simplifies their removal. Identification and removal of these dummy/fake fluxes is critical as saturated flux values can negatively impact continuum finding routines. After determining the wavelength solution and de-Dopplerizing the spectra to bring them to a rest frame, we then apply our novel continuum finding routine described in Algorithm 1. An important point to note is the impact that low signal-to-noise ratios have on

continuum fitting—noisy flux values in a spectrum can easily be confused as true and result in a higher estimation of the continuum compared to its true value. While MARVELS spectra have varying SNRs—both due to the different number of observations stacked to create the final spectrum for a given star, and the fact that the flux for a given star varies widely for different observations due to sky conditions and fibre degradation—our experiments show that for their median value of  $\sim 200$ , this is only a second-order effect. We therefore run Algorithm 1 by assuming an SNR of 200 for all the MARVELS spectra. At the same time we incorporate the variation in SNRs across spectra of MARVELS stars by adding Gaussian noise to PHOENIX spectra before normalization (step (iii) above). Finally, we note that our method is subject to the same limitation as other methods of continuum normalization, in that as we move to lower temperatures, the estimated continuum moves below the true continuum (see Figure 2 in Bialek et al. 2019). These considerations make it critical that the same continuum fitting routine is applied to both synthetic and real spectra, to ensure that both are subject to the same biases.

With the above steps completed, we end up with a total of 110,000 PHOENIX spectra, and 3,075 MARVELS spectra.

## 4 THEORETICAL BACKGROUND

We briefly describe here several advanced deep learning tools that are used in deep – REMAP to achieve the results in §6.

### 4.1 Transfer Learning

In recent years, deep neural networks have become increasingly good at mapping from inputs to outputs, whether they are images, sentences, or time series. However, this paradigm of *supervised learning*, by virtue of its dependence on large amounts of labeled inputs, is not only data hungry, it is also limiting in the ability to generalize to conditions or data samples that are different from the ones encountered during training. This type of learning is by design isolated and occurs purely based on specific tasks and datasets, and training different, isolated models on each. No knowledge is retained which can be transferred from one model to another.

*Transfer learning* and related domain adaptation techniques (Gilda et al. 2024) allow us to deal with these scenarios by leveraging the already existing labeled data of some related task or domain. We store the knowledge gained from solving the *source task* using the *source data*, and apply it to solve the *target task* of interest using *target data*. This allows us to tackle the dual problems of sparsity and incompleteness in the *target data*. In this work, we use transfer learning to probabilistically predict stellar atmospheric parameters for suspected giant stars in the MARVELS survey.

While several details of how CNNs work so well are still a matter of active research (Zeiler & Fergus 2014; Olah et al. 2017; Bau et al. 2017; Kim et al. 2018), one thing that we are sure of is that lower layers capture low-level image features such as edges, while higher layers focus more on complex details, such as specific compositional features (Krizhevsky et al. 2012). In other words, lower layers capture general representations, while higher layers capture dataset specific information. It then follows that for training a DCNN on different (but similar in at least some way) dataset than the one on which it was trained,<sup>2</sup> we can re-use the already

<sup>2</sup> For instance, a neural net for classifying photographs of people into males

---

### Algorithm 1 Continuum Normalization

---

**Input:** a vector of spectrum flux measurements of length  $N$ ,  $\mathbf{Z} = \{z_n\}_{n=1}^N$ .  
**Output:** the normalized spectrum flux vector of length  $N$ ,  $\mathbf{X} = \{x_n\}_{n=1}^N$ .

- 1: Set  $a$  as the maximum quantity of flux values in each bin that are allowed to be larger than the continuum.
- 2: Define the initial continuum estimate,  $\mathbf{C}$ , as a vector of length  $N$  with all elements set to  $10 + \max(\mathbf{Z})$ .
- 3: **for** bin count  $v$  in range  $[2, 11]$  **do**
- 4:   Partition the index vector,  $[1, N]$ , into  $v$  uniform bins. In each partition, determine the center element and place into vector  $\mathbf{H}$ ,  $\mathbf{H} = [N/v/2, \{[N/v/2, N]\}_{n=1+N/v}^N]$
- 5:   **while** the quantity of **true** values in  $\mathbf{C} > \mathbf{Z}$  is greater than  $a$ , **do**
- 6:     **for** bin index  $h$  in a random permuted vector of  $\mathbf{H}$  **do**
- 7:       Create a subset of vector  $\mathbf{C}$  by duplicating indices  $\mathbf{H}$  of  $\mathbf{C}$  into vector  $\mathbf{E}$ .
- 8:       **if**  $\mathbf{C}(h) > \mathbf{Z}(h)$  **then**
- 9:         Lower the continuum estimate in bin  $h$  by multiplying  $\mathbf{E}(h)$  by 0.999.
- 10:       **if**  $v < 5$  **then**
- 11:         Calculate the continuum estimate,  $\mathbf{C}$ , by fitting a  $v - 1$  degree polynomial to  $(\mathbf{H}, \mathbf{E})$  and evaluate at range  $[1, N]$ .
- 12:         To avoid undesired inflections at the continuum edges we perform linear interpolations to force flat edges in the endpoint bins. At the left edge we find the slope between the points  $\mathbf{C}(\mathbf{H}(1))$  and  $\mathbf{C}(\mathbf{H}(1) + 1)$ , then extrapolate to replace the index range  $[1, \mathbf{H}(1) - 1]$ . The right edge is altered in the same manner at the index range  $[\mathbf{H}(v) + 1, N]$ .
- 13:       **else**
- 14:         Calculate the continuum estimate,  $\mathbf{C}$ , by linear interpolation of  $(\mathbf{H}, \mathbf{E})$  and evaluate at range  $[1, N]$ .
- 15:       **end if**
- 16:       **end if**
- 17:     **end for**
- 18:   **end while**
- 19: **end for**
- 20: Calculate the continuum estimate,  $\mathbf{C}$ , by fitting a 6 degree polynomial to  $(\mathbf{H}, \mathbf{E})$  and evaluate at range  $[1, N]$ .
- 21: To avoid undesired inflections at the continuum edges we perform linear interpolations to force flat edges in the endpoint bins. At the left edge we find the slope between the points  $\mathbf{C}(\mathbf{H}(1))$  and  $\mathbf{C}(\mathbf{H}(1) + 1)$ , then extrapolate to replace the index range  $[1, \mathbf{H}(1) - 1]$ . The right edge is altered in the same manner at the index range  $[\mathbf{H}(v) + 1, N]$ .
- 22: To smooth out the linear interpolations performed at the edges the continuum estimate is convolved with a gaussian kernel with sigma of 150.

---

extracted features. In practice, we update the weights and biases of the ‘pre-trained’ model with a small learning rate in order to ensure that we do not unlearn the previously acquired knowledge. This simple approach of *fine-tuning* has been shown to achieve astounding results on an array of vision tasks (Yosinski et al. 2014; Razavian et al. 2014; Girshick et al. 2014; Long et al. 2015).

and females, can be re-tooled to classify photographs of people into different age groups.

In this work, we train deep – REMAP on a large corpus of augmented synthetic PHOENIX absorption spectra that have been pre-processed to match MARVELS characteristics (see §3.3 for details). Once the network achieves convergence (i.e., error on the validation set no longer decreases), we retrain it with a very small layer-dependent learning rate<sup>3</sup> on labeled MARVELS spectra (F,G and K-dwarfs for which we know the atmospheric parameters using spectral indices from Grieves et al. 2018) until convergence. Finally, this re-trained/fin-tuned network is used to make predictions on suspected 732 giants in the MARVELS survey.

## 4.2 Multi-Task Learning

In traditional deep learning, we typically create and train a neural network to optimize performance on one particular task—differentiating cats from dogs, determining the presence or absence of a tumor in an MRI image, predicting the type of solar flares based on spatio-temporal data of the Sun. While it can achieve impressive results on a host of tasks, this paradigm of learning has two disadvantages: (i) to optimize for multiple tasks, we are forced to chain multiple models, each optimized for a single goal; this increase in the number of models leads to a large number of parameters needing to be trained, which increases the chance of over-fitting; and (ii) by focusing on a single task at a time, we ignore shared information that might be prevalent across different tasks, and reduce the generalization ability of our models. An alternative to such *single-task learning* approach is to share representations across inter-related tasks, and thus to enable our model to generalize better on all tasks (Thrun 1996; Caruana 1997; Ando & Zhang 2005). This is the sub-field of *Multi-Task learning* (MTL), which lets us exploit and exploit the commonalities and differences across related tasks.

Caruana (1997) characterized MTL as, “... an approach to inductive transfer that improves generalization by using the domain information contained in the training signals of related tasks as an inductive bias. It does this by learning tasks in parallel while using a shared representation; what is learned for each task can help other tasks be learned better.” Inductive bias forces a model to preferentially select some hypotheses over others. For example, a common form of inductive bias is *l1* regularization, which leads to a preference for sparse solutions. In the case of MTL, the inductive bias is provided by the auxiliary tasks, which cause the model to prefer hypotheses that explain more than one task; this generally leads to solutions that generalize better (Ruder 2017).

While MTL has showed remarkable success across a number of fields—natural language processing (Collobert & Weston 2008), computer vision (Girshick 2015) and cancer discovery (Hajiramezanali et al. 2018)—to the best of our knowledge, this is the first work utilizing MTL in the analysis of stellar spectra. In this paper, we interpret each ‘task’ as the prediction of one of the three stellar parameters, and train our model to simultaneously classify 1D absorption spectra into appropriate bins of effective temperature ( $T_{\text{eff}}$ ), surface gravity ( $\log g$ ), and metallicity ([Fe/H]). We provide the implementation details in §5.

<sup>3</sup> Shallow layers are fine-tuned with the lowest learning rates since they capture the ‘big details’ which are likely to be similar between both PHOENIX and MARVELS spectra; the learning rate is linearly increased with progressively higher layers. See §5 for specific values.

## 4.3 Asymmetric Loss Function

In this work, we have designed deep – REMAP as a classifier (for predicting discrete labels) as opposed to a more intuitive regressor (for predicting continuous, real-valued labels) for two reasons: (i) it makes it easy to generalize the network to work with non-Gaussian distributions of labels (i.e., unlike in Bialek et al. 2019 we are no longer restricted to predicting just the mean and standard deviation of the three labels  $T_{\text{eff}}$ , [Fe/H], and  $\log g$ ); and (ii) it makes it easy to apply an embedding loss such as the triplet loss, and thus makes the model interpretable by enabling the user to query the nearest neighbors in the embedding space. This allows for qualitative assessment of which known spectra the model considers most similar to the input. Once we have discretized the three stellar parameters for use by the model, we are still left with two types of asymmetries:

(i) Arising from imbalanced training data. This refers to the fact that class distributions of the three atmospheric parameters for MARVELS stars are not uniform, which can bias the model towards the label of the majority class. For example, in the absence of any corrective mechanisms, a neural network fine-tuned on such a dataset would be more likely to deduce that the temperature of a previously unseen spectrum is 5800 K than 4200 K or 6900 K.

(ii) Arising from finite, Gaussian distribution of the atmospheric parameters about their mean. By default, classification losses assume a Dirac-delta like distribution of output labels. In other words, when a network with such a loss function sees a stellar spectrum in the training set with temperature 5,000 K, it will try to predict this by assigning a weight of 1.0 to the temperature bin corresponding to 5,000 K, and penalize all other temperature bins equally by assigning them the same weight of 0.0. This is in direct contrast to the Gaussian distribution of properties observed in nature—we know that for the above star, a temperature of 4,850 K is much more likely than temperature of 6,850 K, and hence the bins corresponding to these two temperatures should be penalized differently.

To handle (i) above, we use *focal loss* (Lin et al. 2017) instead of cross-entropy loss. Focal loss intrinsically handles class imbalance by forcing the model to focus more on incorrectly predicted samples and less on correctly predicted ones. To handle (ii), we introduce a cost matrix that asymmetrically penalizes incorrect labels by assigning Gaussian weights, as expounded upon in §5.

## 4.4 Triplet Loss

The most commonly used loss functions, cross-entropy loss for classification and mean squared error loss for regression, aim to predict a discrete or continuous-valued label given an input. While modern convolutional architectures (such as ResNet (He et al. 2016), Inception (Szegedy et al. 2016), and HRNet (Wang et al. 2019)) trained with these losses learn powerful representations, they have limited intra-class compactness—input samples belonging to a given output parameter bin should be close by—and inter-class separation—input samples belonging to different classes should be far away. To boost model skill and generalization in such cases of transfer learning, Taha et al. (2019) demonstrate the importance of regularizing the softmax loss with a *ranking* (or *embedding*) loss. Specifically, they show improved classification performance across a wide variety of datasets when using *triplet loss* (Chechik et al. 2010) in conjunction with softmax loss, in a novel two-headed architecture.

The aim of an embedding loss is to optimize the relative distances between the inputs. A generic embedding loss consists of

three components: embeddings, a similarity score, and the loss function itself. By using the neural network as a feature extractor, we get an embedded representation for each sample in the input. Then we define a similarity score (such as the Euclidean distance), typically taking two or three embedding under consideration at a time. Finally, we train the neural network using the embedding loss function to minimize distances among samples belonging to the same class, and maximize distance among samples belonging to different classes.

This training methodology using triplet loss as the embedding loss function has demonstrated state-of-the-art results in tasks such as person re-identification (Hermans et al. 2017) and face recognition (Schroff et al. 2015). In this paper, we leverage triplet loss as a classification regularizer. It is formulated as (Chechik et al. 2010):

$$L_{\text{triplet}} = \frac{1}{b} \sum_{i=1}^b [D(a_i, p_i) - D(a_i, n_i) + m]_+, \quad (1)$$

where the embedding  $a$  of a reference (*anchor*) image is pushed closer to the embedding  $p$  of a *positive* image (image belonging to the same class as the anchor) than it is to the embedding  $n$  of an image from a different class. For the distance function  $D$  we use the  $l2$  norm (Euclidean distance). The final loss function that we optimize for a given stellar parameter is:

$$L = L_{\text{softmax}} + \lambda L_{\text{triplet}} \quad (2)$$

$L_{\text{softmax}}$  is the standard softmax loss defined as:

$$L_{\text{softmax}} = - \sum_{i=1}^b \log \frac{\exp(\mathbf{z}_i)}{\sum_{\text{classes}} \exp(\mathbf{z}_i)}, \quad (3)$$

where  $b$  is the batch-size.  $\lambda$  is the regularization parameter found through cross-validation. Their values are defined in §5.

#### 4.5 Temperature Scaling

To be reliable, classification networks must not only be accurate, but also be knowledgeable of their own chances of being incorrect. That is, a classifier’s predicted probability estimates associated with a class label should be representative of the true correctness likelihood. This *confidence calibration* not only helps reduce model bias, it is also important for model interpretability (Gilda et al. 2021a, 2020). Guo et al. (2017) found that as neural networks have become larger, deeper, and more accurate with time, they have also become more poorly calibrated than their older, smaller cousins. Specifically, they find that model capacity is directly correlated with degree of over-confidence of a model in its predictions. They offer a simple and effective prescription to this problem—*temperature scaling*. It works by re-scaling the outputs  $\mathbf{z}$  of the logits (inputs to the last, softmax layer of a classifier) by a scalar  $T$ ; that is,  $\mathbf{z} \rightarrow \frac{\mathbf{z}}{T}$  in Equation 3.

While Guo et al. (2017) suggest using hyperparameter optimization (HPO) to determine the scaling parameter  $T$ , we modify their algorithm by creating a custom layer with  $T$  as a learnable parameter. This significantly reduces the expensive computational overhead associated with HPO.

#### 4.6 Cosine Annealing for Learning

Gradient-based optimization algorithms such as Stochastic Gradient Descent (SGD, Zhang 2004) and Adam (Kingma & Ba 2014) require the user to set the learning rate—the most important hyperparameter for training deep neural networks (Smith 2018; Smith &

Topin 2019). The *learning rate schedule* (learning rate as a function of epochs) is primarily responsible for determining how fast and how well the network is able to converge to a good local minimum. The most commonly used method to set the learning rate schedule is to choose a good starting number (one that results in a steep and smooth decline of both the training and the validation error) by trial and error, and to reduce it over time when the training error/accuracy plateaus. This method results in two issues (Smith 2017): (i) picking the right value for the learning rate often ends up becoming more of an art than a science, and can be both time-consuming and sub-optimal; and (ii) even with good values for the model hyper-parameters, training deep neural networks often takes a very long time.

To tackle these problems, we use a recently introduced cyclical learning rate policy (Smith 2017, 2018; Smith & Topin 2019) called *cosine annealing* (Loshchilov & Hutter 2016). We start training with a very small learning rate and increase it exponentially at every iteration. We terminate training when the training loss starts to increase drastically. We then plot the loss function against the learning rate, and pick a value a little lower than that corresponding to the loss minimum—this is the point where the loss is both low and still decreasing. This is the highest learning rate we use in our policy. We set the lowest rate to be a factor of 100 smaller. With these two limits specified, we define our learning rate policy as the cosine annealing function suggested by Loshchilov & Hutter (2016). This cyclical learning rate policy has been shown to help gradient-based optimization algorithms escape from saddle points much quicker (Dauphin et al. 2015; Bengio et al. 2017).

#### 4.7 Stochastic Weight Averaging

The goal of any ML task is to find a model that will best explain the relationship between the dependent and independent variables, and consequently predict the former given a new, unseen sample of the latter. One approach to this is to tune the hyperparameters of the model and pick the set that result in the best performance on the validation set—at the cost of spending significant time and computational resources. While this can often boost model performance, it still leaves us prone to the biases and the peculiarities of the specific ML or DL algorithm under consideration. An alternative to this is to leverage the ‘wisdom of the crowds’. Ensembling is a method where we combine the predictions of several base models on the same input and average them in some way to determine the final prediction. These different models can either be separate, individual architectures, different realizations of the same architecture with different hyperparameters, different realizations of the same architecture with different initializations (Lakshminarayanan et al. 2017), or some combinations of these (Ju et al. 2018). The way of averaging can either be simple voting, weighted voting, or using another model that takes as inputs the predictions of the original models (stacking, Ju et al. 2018). All these methods are ensembles in the *model space*, in that they combine several models and use their predictions to produce the final prediction. They all share a common drawback in that they require multiple models (or iterations of the same model) to be trained, which is both demanding in terms of time consumption and memory footprint (to save the weights and parameters of the different models).

Stochastic Weight Averaging (SWA, Izmailov et al. 2018) is a novel, alternative way of ensembling deep neural networks in the *weights space*. It produces an ensemble by combining the weights of the same network at different stages of training and then uses the model with the combined weights to make predictions. SWA

is easy to implement, improves generalization, and has a trivial computational cost since we only need two models—the base model, and the other running average of the weights of the base model. This is described in detail in §5.

SWA has been shown to significantly improve generalization in computer vision tasks, using diverse neural network architectures such as VGG, ResNets, Wide ResNets and DenseNets, on popular benchmark datasets such as ImageNet, CIFAR-10, and CIFAR-100 (Athiwaratkun et al. 2018; Izmailov et al. 2018). In this paper, we use SWA with cosine annealing (see §4.6).

## 5 IMPLEMENTATION DETAILS

The deep – REMAP architecture introduced in §2 is illustrated in Figure 1. The left sub-figure depicts the structure of a single residual module, the middle sub-figure depicts the ‘body’ of the network, comprising of multiple such residual modules, and the right sub-figure depicts the multi-headed structure whence we obtain probabilistic predictions for the three stellar parameters. We have designed our model as a classifier, and hence the very first step in the training process is to convert the continuous-valued stellar parameters into discrete valued bins. For clarity we describe this process for  $T_{\text{eff}}$  (extension to the other two stellar parameters is trivial), which we illustrate in a forthcoming figure.

(i) First, we calculate the median uncertainty value for  $T_{\text{eff}}$  for the 30 MARVELS calibration stars, which is 80 K. This determines the bin size when we discretize  $T_{\text{eff}}$  in the next step.

(ii) Next, we one-hot encode (§2)  $T_{\text{eff}}$  values for all spectra (110,000 from PHOENIX, and 2,343 from MARVELS). As a result, the parameter space for  $T_{\text{eff}}$  (3,000 K–7,000 K, see §3.2) is discretized into 50 bins of size  $\Delta T_{\text{eff}} = 80$  K each.

(iii) We then convert the discrete  $T_{\text{eff}}$  values for PHOENIX spectra into Gaussian distributions. We assume that instead of being discretely valued, the temperature values are sharp peaked Gaussians, with the difference between two consecutive peaks being equal to  $5\sigma$ . Since the temperatures are equally spaced at 100 K, this sets  $\sigma_{\text{PHOENIX}}$  at 20 K. Since label values for MARVELS spectra already have uncertainties, this step is not applied to them.

(iv) We employ *asymmetric label smoothing* (Szegedy et al. 2016; Müller et al. 2019) to model the uncertainties in  $T_{\text{eff}}$  (point (ii) in §4.3). Specifically, we superimpose the probability distribution function for  $T_{\text{eff}}$  for a given spectrum on its binned histogram from step (ii) above, and add up the values in each bin. For the specific case of a Gaussian distribution with mean  $\mu$  and standard deviation  $\sigma$ , we take advantage of the analytical formula for its cumulative distribution function (CDF)<sup>4</sup>:

$$T_{\text{eff},i} = \text{erf} \left( \frac{T_{\text{eff},i-r} - \mu}{\sigma\sqrt{2}} \right) - \text{erf} \left( \frac{T_{\text{eff},i-l} - \mu}{\sigma\sqrt{2}} \right), \quad (4)$$

where the value in a bin  $i$  is the difference of the CDF of the distribution at the left edge of the bin (subscript  $i-l$  in the above equation) from the CDF at the right edge (subscript  $i-r$ ).

(v) For any given spectrum, the binned  $T_{\text{eff}}$  values now represent the probability mass function (PMF) of its effective temperature. We convert this to a cost vector by subtracting the values from 1. This informs the neural network that for a spectrum with  $T_{\text{eff}} = 5,000$  K, for instance, the cost of predicting its temperature at 5,000 K is much lower than the cost of predicting it at 6,000 K.

<sup>4</sup>  $\text{cdf}(x) = \frac{1}{2} \left[ 1 + \text{erf} \left( \frac{x-\mu}{\sigma\sqrt{2}} \right) \right]$

After altering the labels and the cost functions, we focus our attention on the spectral flux values. We begin by pre-processing, augmenting, and continuum normalizing the PHOENIX spectra as described in §3.3, and consequently create two sets—Set I where these spectra are trimmed to lie in the wavelength range of 4850 to 5280 Å, and Set II with the trimmed wavelength range of 5280 to 5750 Å. These correspond to the wavelength ranges of the two ‘beams’ of MARVELS (Grieves et al. 2018); by creating two sets, we make the network capable of capturing information from, and making predictions on, spectra from both beams.

We begin by using PHOENIX Set I, and correspondingly MARVELS beam A. We train deep – REMAP in two phases: first on the 110,000 pre-processed and augmented PHOENIX spectra, then on the 2,313 continuum-normalized MARVELS spectra (see §3.1) to fine-tune it. We set the number of residual units and the number of filters in each by employing 10-fold cross validation—cyclically training on 90% of the spectra, and reporting the results on the remaining 10%, choosing the aforementioned hyperparameters such that the mean of the final loss,  $L_{\text{final}}$ , across all 10 folds is minimized.

The upper and lower learning rate limits of 1e-3 and 1e-5 for the pre-training phase are obtained by following the procedure outlined in §4.6. For the fine-tuning phase, the learning rates are obtained as such:

(i) For the ‘heads’—consisting of two fully connected, one temperature scaling (§4.5), and global pooling layers<sup>5</sup>—of each of the three stellar parameters (Figure 1), the upper and lower limits are reduced to  $\frac{1}{10}$  of their pre-training values.

(ii) For each of the residual modules, the upper and lower limits are reduced by a factor of  $\frac{1}{10^i}$  of their respective values, where  $i$  is the count of a module from the ‘head’, the latter having  $i$  of 1. For instance, for the rightmost module in Figure 1, this factor is  $\frac{1}{20}$ , for the second to the rightmost module it is  $\frac{1}{30}$ , and so on.

This graded reduction in learning rates for the second phase of fine-tuning preserves the most amount of knowledge in the shallowest layers, and allows the quickest change for the deepest layers. We empirically set the number of epochs per cycle and the number of cycles at 30 and 4, respectively.

Stochastic Weight Averaging (SWA, §4.7) is employed for ensembling. At each of the four lowest points of a cycle, we record the model weights  $w$  and create a running average,  $w_{\text{SWA}}$  as follows<sup>6</sup>:

$$w_{\text{SWA}} \leftarrow \frac{w_{\text{SWA}} n_{\text{cycles}} + w_{\text{cycle}}}{n_{\text{cycles}} + 1}, \quad (5)$$

where  $w_{\text{cycle}}$  is the weight of our model at the end of a cycle,  $n_{\text{cycles}}$  is the number of cycles completed, and  $w_{\text{SWA}}$  is initialized to the weights at the end of the first cycle. For prediction, we set the weights of deep – REMAP to the final  $w_{\text{SWA}}$ .

We test our model’s performance by predicting the parameters of the 30 calibration stars from MARVELS. We do this separately for spectra from ‘beam’ A and ‘beam’ B. Finally, we combine both sets of predictions via *conflation*: (Hill & Miller 2011):

$$y_{i, \text{final}} = \frac{y_{i, \text{SetI}} \cdot y_{i, \text{SetII}}}{\sum_j y_{j, \text{SetI}} \cdot y_{j, \text{SetII}}}, \quad (6)$$

where  $y_{i, \text{SetI}}$  is the predicted stellar parameter  $y$ ’s probability in bin  $i$  from Set I (beam A), and the sum in the denominator is over

<sup>5</sup> these are, by definition, non-trainable

<sup>6</sup> <https://pechyonkin.me/stochastic-weight-averaging/>

all bins. [Hill & Miller \(2011\)](#) show that this method of combining probabilistic distributions is superior to simple averaging.

Our final loss function is a linear combination of the regularized loss function in Equation 2 for each of the three stellar parameters:

$$L_{final} = L_{T_{eff}, \text{softmax}} + \lambda_{T_{eff}} L_{T_{eff}, \text{triplet}} + L_{\log g, \text{softmax}} + \lambda_{\log g} L_{\log g, \text{triplet}} + L_{[\text{Fe}/\text{H}], \text{softmax}} + \lambda_{[\text{Fe}/\text{H}]} L_{[\text{Fe}/\text{H}], \text{triplet}} \quad (7)$$

The three  $\lambda$ s are empirically chosen to be 0.001. For model development, we use Keras 2.3.0 ([Chollet 2015](#)) with a Tensorflow 2.0 ([Abadi et al. 2015](#)) backend. On a 24Gb Nvidia Titan RTX GPU, training for phase one takes 45 minutes, while training for the fine-tuning phase takes 5 minutes. Inference time on the 30 calibration stars is negligible.

## 6 RESULTS

We evaluate the performance of the final fine-tuned deep – REMAP model on two test sets: the 30 MARVELS calibration stars with well-determined literature parameters ([Ghezzi et al. 2014](#)), and the 732 FGK giant candidates for which we provide the first parameter estimates. All results shown here are from the combined predictions of the two MARVELS beams, using the conflation method described in Equation 6.

### 6.1 Proof-of-Concept: Model Learning and Feature Separation

Before assessing quantitative performance, we first demonstrate that the network successfully learns to extract physically meaningful features from the spectra. We visualize the network’s high-dimensional embedding space by projecting it onto two dimensions using the t-SNE algorithm ([van der Maaten & Hinton 2008](#)).

Figure 2 shows the evolution of the embedding space for the PHOENIX \*\*training set\*\*. At Epoch 0, the classes are mixed, but by Epoch 50, the triplet loss has successfully organized the spectra into distinct, well-separated clusters for all three stellar parameters. To ensure this is a result of true learning and not merely memorization, we perform the same visualization for the unseen \*\*validation set\*\* in Figure 3. The clear formation of distinct clusters in the validation data confirms that the network has learned generalizable features that correlate with the physical properties of the stars.

### 6.2 Performance on Calibration Stars

Having confirmed the model’s learning capability, we quantify its precision and accuracy against the 30 MARVELS calibration stars. Figure 4 plots our predictions against their established literature values. The model shows excellent agreement, with most predictions falling tightly along the one-to-one line.

Table 1 summarizes the quantitative performance metrics. We report the mean error ( $\mu_\Delta$ ) to assess any systematic bias and the standard deviation of the residuals ( $\sigma_\Delta$ ) as a measure of the prediction scatter. The low bias and small scatter across all three parameters confirm the model’s high fidelity.

**Table 1.** Performance statistics for the 30 calibration stars.  $\mu_\Delta$  is the mean difference (Predicted - True) and  $\sigma_\Delta$  is the standard deviation of the differences.

Parameter	$\mu_\Delta$ (Bias)	$\sigma_\Delta$ (Scatter)
$T_{eff}$ (K)	-10 K	75 K
$\log g$ (dex)	+0.02 dex	0.12 dex
$[\text{Fe}/\text{H}]$ (dex)	-0.01 dex	0.08 dex

### 6.3 Parameterization of FGK Giant Candidates

Applying our validated model to the 732 FGK giant candidates, we find that approximately 80% have parameters consistent with giant or sub-giant classifications. The remaining 20% are classified as dwarfs, consistent with the expected giant contamination rate for the MARVELS survey ([Paegert et al. 2015](#)). An analysis of these re-classified dwarfs reveals no significant trend with signal-to-noise ratio; instead, they appear to be genuine contaminants that the original target selection method failed to remove. A full catalog of the derived parameters for all 732 stars is available as supplementary material.

### 6.4 Ablation Study: Justifying Model Complexity

To justify the inclusion of our advanced components, we performed a brief ablation study. We trained two alternate models: (1) one without the triplet loss regularizer, relying only on focal loss ([Lin et al. 2017](#)), and (2) one without multi-tasking, using three separate networks. The model without triplet loss showed a ~15% increase in scatter for  $\log g$ , indicating a less organized embedding space. The three separate networks required nearly triple the training time and showed degraded performance, confirming that the multi-task architecture effectively leverages shared information between the parameters to improve results, as theorized by [Caruana \(1997\)](#). This demonstrates that both the triplet loss and multi-task learning are crucial components of deep – REMAP’s performance.

## 7 CONCLUSIONS AND DISCUSSION

In this work, we have presented a novel neural network, deep – REMAP, for spectral analysis of 1D spectra, and used it to parameterize MARVELS targets. To the best of our knowledge, this is the first automated model for stellar parameter estimation incorporating a full suite of state-of-the-art deep learning practices, namely transfer learning, multi-task learning, temperature scaling ([Guo et al. 2017](#)), focal loss ([Lin et al. 2017](#)), triplet loss ([Chechik et al. 2010](#)), stochastic weight averaging ([Izmailov et al. 2018](#)), and cosine annealing-based learning rates ([Loshchilov & Hutter 2016](#)). We have shown that with appropriate data augmentation and transfer learning, a network trained primarily on synthetic spectra can be made immune to many observational peculiarities of a given spectrograph and be used for reliable parameter estimation from real observed spectra. We have also shown how a regression-as-classification framework can capture non-Gaussian parameter distributions, while the inclusion of an embedding loss improves both classification and model interpretability. Using this framework, we have predicted, for the first time, the atmospheric parameters and associated uncertainties for 732 MARVELS FGK giant candidates.

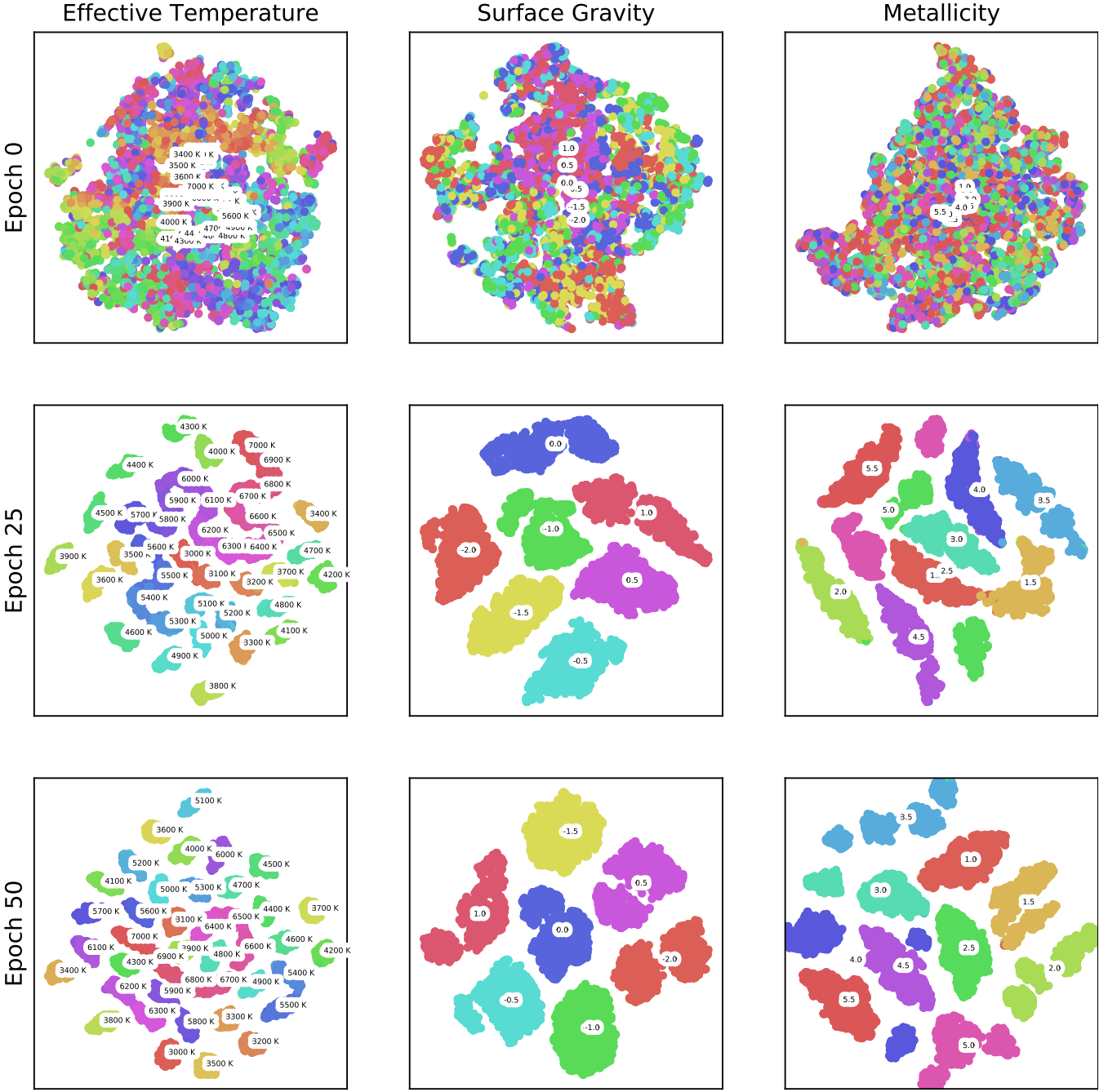


**Figure 2.** Visualization of the learned embedding space for the PHOENIX **training** set at Epoch 0, 25, and 50, projected using t-SNE. Columns from left to right correspond to classes for  $T_{\text{eff}}$ ,  $\log g$ , and  $[\text{Fe}/\text{H}]$ . The clear formation of distinct clusters by Epoch 50 demonstrates that the network is successfully learning to structure the feature space.

### 7.1 Limitations and Future Work

Despite the model's success, we identify areas for future improvement. Our derived metallicity distribution for the giant candidates shows a systematic offset compared to expectations for the solar neighborhood. We suspect this may be due to residual issues in the MARVELS wavelength solution, a challenge noted in previous analyses of the survey data (Grieves et al. 2018). Future work with improved data reduction pipelines may eliminate these systematics. Furthermore, we plan to extend this framework into a fully Bayesian

context by placing priors on the network weights, which would allow for the recovery of full posterior distributions for the stellar parameters instead of binned probabilities. Finally, the flexibility of deep – REMAP will be tested by incorporating other synthetic spectral libraries and applying it to different large-scale surveys, pushing towards the prediction of detailed elemental abundances.

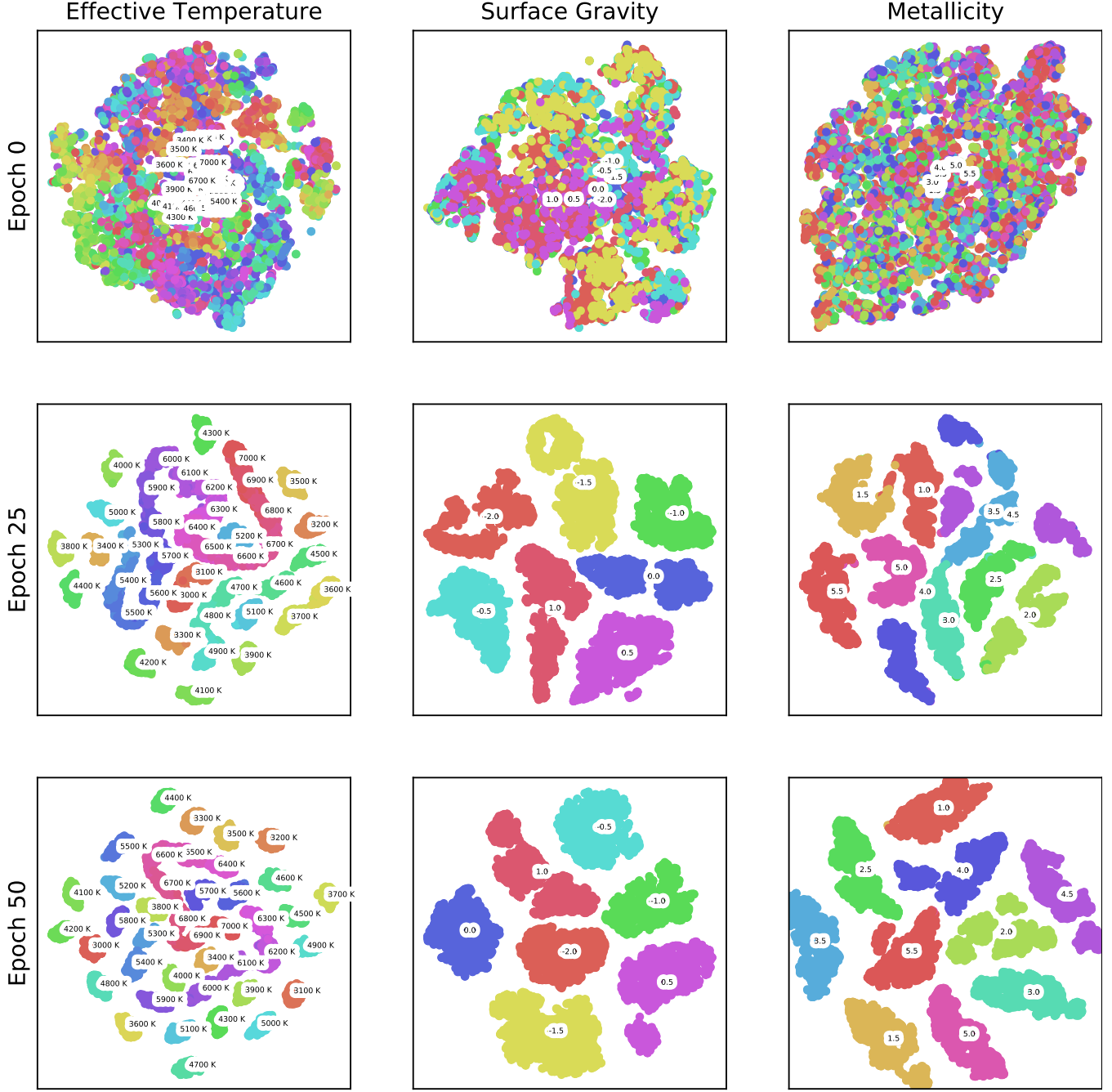


**Figure 3.** Same as Figure 2, but for the unseen PHOENIX **validation** set. The emergence of well-separated clusters in this hold-out sample confirms that the model is not overfitting and has learned generalizable features, validating the effectiveness of our training methodology.

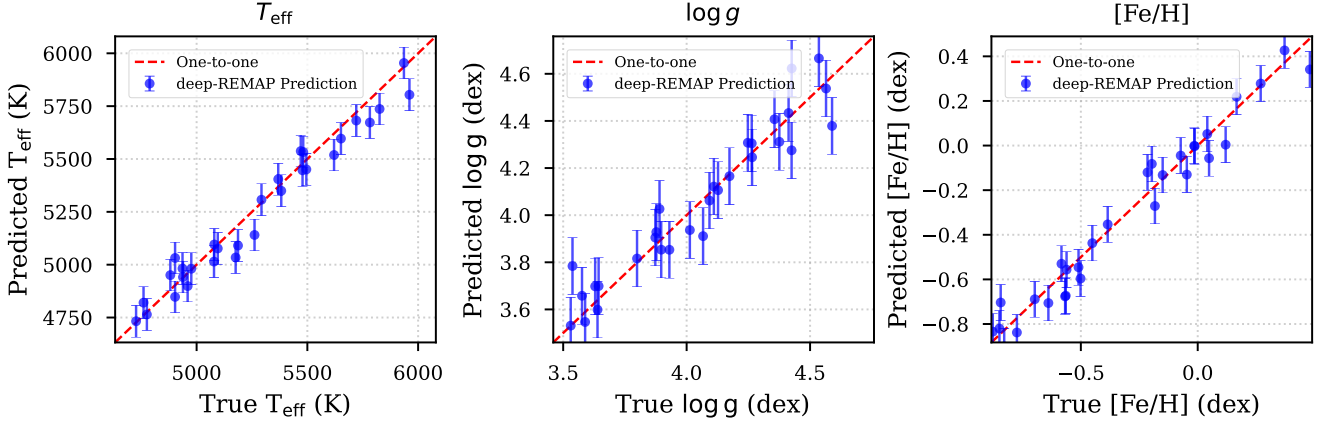


**Figure 4.** Comparison of our deep – REMAP predicted parameters versus the known literature values for the 30 MARVELS calibration stars (Ghezzi et al. 2014). From left to right: effective temperature ( $T_{\text{eff}}$ ), surface gravity ( $\log g$ ), and metallicity ( $[\text{Fe}/\text{H}]$ ). The blue points show the median of our predicted probability distribution, with error bars representing the 16th and 84th percentiles. The dashed red line indicates the one-to-one correspondence. The tight clustering around this line demonstrates the high accuracy and precision of our model.

## ACKNOWLEDGEMENTS

Research for this paper was undertaken when the author was a graduate assistant in the Department of Astronomy, University of Florida. We would like to thank the anonymous reviewers for their detailed and constructive feedback which significantly improved the quality of this manuscript. We also thank Dr. Jian Ge, and Mr. Nolan Grieves, for helpful discussions and feedback. This research has made use of NASA’s Astrophysics Data System. The author declares no conflicts of interest.

## DATA AVAILABILITY

The specific data underlying this article, and the code used to train the deep – REMAP model will be shared on a case-by-case basis by the corresponding author. The MARVELS data are available through the SDSS archives, and the PHOENIX spectra are available at the Göttingen Spectral Library.

## REFERENCES

Abadi M., et al., 2015, TensorFlow: Large-Scale Machine Learning on Heterogeneous Systems, <http://tensorflow.org/>

Alam S., et al., 2015, The Astrophysical Journal Supplement Series, 219, 12

Ando R. K., Zhang T., 2005, Journal of Machine Learning Research, 6, 1817

Athiwaratkun B., Finzi M., Izmailov P., Wilson A. G., 2018, arXiv preprint arXiv:1806.05594

Bailer-Jones C. A., 2000, arXiv preprint astro-ph/0003071

Bau D., Zhou B., Khosla A., Oliva A., Torralba A., 2017, in Proceedings of the IEEE conference on computer vision and pattern recognition. pp 6541–6549

Bengio Y., Goodfellow I., Courville A., 2017, Deep learning. Citeseer

Bialek S., Fabbro S., Venn K. A., Kumar N., O’Brian T., Yi K. M., 2019, arXiv preprint arXiv:1911.02602

Caruana R., 1997, Machine learning, 28, 41

Casey A. R., Hogg D. W., Ness M., Rix H.-W., Ho A. Q., Gilmore G., 2016, arXiv preprint arXiv:1603.03040

Chechik G., Sharma V., Shalit U., Bengio S., 2010, Journal of Machine Learning Research, 11, 1109

Chollet F., 2015, keras, <https://github.com/fchollet/keras>

Ciardi D. R., et al., 2011, The Astronomical Journal, 141, 108

Collobert R., Weston J., 2008, in Proceedings of the 25th international conference on Machine learning. pp 160–167

Cui X.-Q., et al., 2012, Research in Astronomy and Astrophysics, 12, 1197

Dauphin Y., De Vries H., Bengio Y., 2015, in Advances in neural information processing systems. pp 1504–1512

Dawson K. S., et al., 2012, The Astronomical Journal, 145, 10

De Laverny P., Recio-Blanco A., Worley C., Plez B., 2012, Astronomy & Astrophysics, 544, A126

Eisenstein D. J., et al., 2011, The Astronomical Journal, 142, 72

Franchini M., et al., 2018, The Astrophysical Journal, 862, 146

Ge J., et al., 2008, in Extreme Solar Systems. p. 449

Ge J., et al., 2009, in Shaklan S. B., ed., Proceedings of the SPIE Vol. 7440, Techniques and Instrumentation for Detection of Exoplanets IV. SPIE, pp 187–196, doi:10.1117/12.826651

Ghezzi L., et al., 2014, The Astronomical Journal, 148, 105

Gilda S., Slepian Z., 2019, *Monthly Notices of the Royal Astronomical Society*, 490, 5249

Gilda S., et al., 2020, in 34th conference on Neural Information Processing Systems. Virtual conference, United States, <https://hal.science/hal-03080075>

Gilda S., et al., 2021a, *Monthly Notices of the Royal Astronomical Society*, 510, 870

Gilda S., Lower S., Narayanan D., 2021b, The Astrophysical Journal, 916, 43

Gilda S., de Mathelin A., Bellstedt S., Richard G., 2024, *Astronomy*, 3, 189

Gilmore G., et al., 2012, The Messenger, 147, 25

Girshick R., 2015, in Proceedings of the IEEE international conference on computer vision. pp 1440–1448

Girshick R., Donahue J., Darrell T., Malik J., 2014, in Proceedings of the IEEE conference on computer vision and pattern recognition. pp 580–587

Glorot X., Bordes A., Bengio Y., 2011, in Proceedings of the fourteenth international conference on artificial intelligence and statistics. pp 315–323

Grieves N., et al., 2017, *Monthly Notices of the Royal Astronomical Society*, 467, 4264

Grieves N., et al., 2018, *Monthly Notices of the Royal Astronomical Society*, 481, 3244

Gunn J. E., et al., 2006, *The Astronomical Journal*, 131, 2332

Guo C., Pleiss G., Sun Y., Weinberger K. Q., 2017, in *Proceedings of the 34th International Conference on Machine Learning - Volume 70. ICML 2017. JMLR.org*, pp 1321–1330

Hahnloser R. H., Sarpeshkar R., Mahowald M. A., Douglas R. J., Seung H. S., 2000, *Nature*, 405, 947

Hajiramezanal E., Dadaneh S. Z., Karbalayghareh A., Zhou M., Qian X., 2018, in *Advances in Neural Information Processing Systems*. pp 9115–9124

He K., Zhang X., Ren S., Sun J., 2016, in *Proceedings of the IEEE conference on computer vision and pattern recognition*, pp 770–778

Hermans A., Beyer L., Leibe B., 2017, arXiv preprint arXiv:1703.07737

Hill T. P., Miller J., 2011, *Chaos: An Interdisciplinary Journal of Nonlinear Science*, 21, 033102

Ho A. Y. Q., et al., 2017, *The Astrophysical Journal*, 836, 5

Hoffer E., Ailon N., 2015, in *International Workshop on Similarity-Based Pattern Recognition*. pp 84–92

Hoyle B., 2016, *Astronomy and Computing*, 16, 34

Husser T.-O., Wende-von Berg S., Dreizler S., Homeier D., Reiners A., Barman T., Hauschildt P. H., 2013, *Astronomy & Astrophysics*, 553, A6

Ioffe S., Szegedy C., 2015, arXiv preprint arXiv:1502.03167

Ivezić Ž., et al., 2019, *The Astrophysical Journal*, 873, 111

Izmailov P., Podoprikin D., Garipov T., Vetrov D., Wilson A. G., 2018, arXiv preprint arXiv:1803.05407

Ju C., Bibaut A., van der Laan M., 2018, *Journal of Applied Statistics*, 45, 2800

Kim E. J., Brunner R. J., 2016, *Monthly Notices of the Royal Astronomical Society*, p. stw2672

Kim B., Wattenberg M., Gilmer J., Cai C., Wexler J., Viegas F., Sayres R., 2018, in *International conference on machine learning*. pp 2668–2677

Kingma D. P., Ba J., 2014, arXiv preprint arXiv:1412.6980

Kordopatis G., et al., 2013, *The Astronomical Journal*, 146, 134

Krizhevsky A., Sutskever I., Hinton G. E., 2012, in *Advances in neural information processing systems*. pp 1097–1105

Lakshminarayanan B., Pritzel A., Blundell C., 2017, in *Advances in Neural Information Processing Systems*. pp 6402–6413

Lanusse F., Ma Q., Li N., Collett T. E., Li C.-L., Ravanbakhsh S., Mandelbaum R., Póczos B., 2017, *Monthly Notices of the Royal Astronomical Society*, 473, 3895

LeCun Y., Bottou L., Bengio Y., Haffner P., et al., 1998, *Proceedings of the IEEE*, 86, 2278

Lee Y. S., et al., 2008, *The Astronomical Journal*, 136, 2022

Leung H. W., Bovy J., Mackereth J. T., Miglio A., 2023, *MNRAS*, 522, 4577

Levi M., et al., 2013, arXiv preprint arXiv:1308.0847

Li J., Wong K. W. K., Hogg D. W., Rix H.-W., Chandra V., 2024, *ApJS*, 272, 2

Lin M., Chen Q., Yan S., 2013, arXiv preprint arXiv:1312.4400

Lin T.-Y., Goyal P., Girshick R., He K., Dollár P., 2017, in *Proceedings of the IEEE international conference on computer vision*. pp 2980–2988

Long J., Shelhamer E., Darrell T., 2015, in *Proceedings of the IEEE conference on computer vision and pattern recognition*. pp 3431–3440

Loshchilov I., Hutter F., 2016, arXiv preprint arXiv:1608.03983

Ma B., et al., 2018, *Monthly Notices of the Royal Astronomical Society*, 480, 2411

Maas A. L., Hannun A. Y., Ng A. Y., 2013, in *in ICML Workshop on Deep Learning for Audio, Speech and Language Processing*.

Mahabal A., et al., 2019, *Publications of the Astronomical Society of the Pacific*, 131, 038002

Manteiga M., Ordóñez D., Dafonte C., Arcay B., 2010, *Publications of the Astronomical Society of the Pacific*, 122, 608

Misra D., 2019, arXiv preprint arXiv:1908.08681

Müller R., Kornblith S., Hinton G., 2019, arXiv preprint arXiv:1906.02629

Nair V., Hinton G. E., 2010, in *Proceedings of the 27th international conference on machine learning (ICML-10)*. pp 807–814

Ness M., Hogg D. W., Rix H.-W., Ho A. Y., Zasowski G., 2015, *The Astrophysical Journal*, 808, 16

O'Briain T., Ting Y.-S., Fabbro S., Yi K. M., Venn K., Bialek S., 2021, *ApJ*, 906, 130

Olah C., Mordvintsev A., Schubert L., 2017, *Distill*, 2, e7

Paegert M., et al., 2015, *The Astronomical Journal*, 149, 186

Pérez A. E. G., et al., 2016, *The Astronomical Journal*, 151, 144

Razavian A. S., Azizpour H., Sullivan J., Carlsson S., 2014, in *Proceedings of the IEEE conference on computer vision and pattern recognition workshops*. pp 512–519

Ruder S., 2017, arXiv preprint arXiv:1706.05098

Schmidhuber J., 2015, *Neural networks*, 61, 85

Schroff F., Kalenichenko D., Philbin J., 2015, in *Proceedings of the IEEE conference on computer vision and pattern recognition*. pp 815–823

Sharma K., Kembhavi A., Kembhavi A., Sivarani T., Abraham S., Vaghmare K., 2019, *Monthly Notices of the Royal Astronomical Society*, 491, 2280

Smith L. N., 2017, in *2017 IEEE Winter Conference on Applications of Computer Vision (WACV)*. pp 464–472

Smith L. N., 2018, arXiv preprint arXiv:1803.09820

Smith L. N., Topin N., 2019, in *Artificial Intelligence and Machine Learning for Multi-Domain Operations Applications*. p. 1100612

Smolinski J. P., et al., 2011, *The Astronomical Journal*, 141, 89

Snider S., Prieto C. A., von Hippel T., Beers T. C., Sneden C., Qu Y., Rossi S., 2001, *The Astrophysical Journal*, 562, 528

Sousa S. G., 2014, in Niemczura E., Smalley B., Pych W., eds., *Determination of Atmospheric Parameters of B-, A-, F- and G-Type Stars: Lectures from the School of Spectroscopic Data Analyses*. Springer International Publishing, Cham, pp 297–310, doi:10.1007/978-3-319-06956-2\_26, [https://doi.org/10.1007/978-3-319-06956-2\\_26](https://doi.org/10.1007/978-3-319-06956-2_26)

Srivastava N., Hinton G., Krizhevsky A., Sutskever I., Salakhutdinov R., 2014, *The journal of machine learning research*, 15, 1929

Szegedy C., Vanhoucke V., Ioffe S., Shlens J., Wojna Z., 2016, in *Proceedings of the IEEE conference on computer vision and pattern recognition*. pp 2818–2826

Taha A., Chen Y.-T., Misu T., Davis L., 2019, arXiv preprint arXiv:1901.08616

Thomas N., 2015, *Effect of metallicity on giant planet and brown dwarf formation*

Thomas N., Ge J., Grieves N., Li R., Sithajan S., 2016, *Publications of the Astronomical Society of the Pacific*, 128, 045003

Thrun S., 1996, in *Advances in neural information processing systems*. pp 640–646

Ting Y.-S., Conroy C., Rix H.-W., Cargile P., 2018, arXiv preprint arXiv:1804.01530

Valenti J. A., Fischer D. A., 2005, *The Astrophysical Journal Supplement Series*, 159, 141

Wang H., Li S., Luo A., 2010, in *2010 3rd International Congress on Image and Signal Processing*. pp 1045–1048, doi:10.1109/CISP.2010.5646929

Wang J., et al., 2019, arXiv preprint arXiv:1908.07919

Worley C., de Laverny P., Recio-Blanco A., Hill V., Bijaoui A., Ordenovic C., 2012, *Astronomy & Astrophysics*, 542, A48

Xiang M.-S., et al., 2016, *Monthly Notices of the Royal Astronomical Society*, 464, 3657

Yanny B., et al., 2009, *The Astronomical Journal*, 137, 4377

York D. G., et al., 2000, *The Astronomical Journal*, 120, 1579

Yosinski J., Clune J., Bengio Y., Lipson H., 2014, in *Advances in neural information processing systems*. pp 3320–3328

Zeiler M. D., Fergus R., 2014, in *European conference on computer vision*. pp 818–833

Zhang T., 2004, in *Proceedings of the twenty-first international conference on Machine learning*. p. 116

Zhao R., Luo A., 2006, *Guang pu xue yu guang pu fen xi= Guang pu*, 26, 587

van der Maaten L., Hinton G., 2008, *Journal of Machine Learning Research*, 9, 2579